

# Complete Wetting of Pits and Grooves

M. Tasinkevych<sup>1,2</sup> and S. Dietrich<sup>1,2</sup>

<sup>1</sup>Max-Planck-Institut für Metallforschung, Heisenbergstr. 3, D-70569 Stuttgart, Germany

<sup>2</sup>Institut für Theoretische und Angewandte Physik,  
Universität Stuttgart, Pfaffenwaldring 57, D-70569 Stuttgart, Germany

(Dated: March 7, 2018)

For one-component volatile fluids governed by dispersion forces an effective interface Hamiltonian, derived from a microscopic density functional theory, is used to study complete wetting of geometrically structured substrates. Also the long range of substrate potentials is explicitly taken into account. Four types of geometrical patterns are considered: (i) one-dimensional periodic arrays of rectangular or parabolic grooves and (ii) two-dimensional lattices of cylindrical or parabolic pits. We present numerical evidence that at the centers of the cavity regions the thicknesses of the adsorbed films obey precisely the same geometrical covariance relation, which has been recently reported for complete cone and wedge filling. However, this covariance does not hold for the laterally averaged wetting film thicknesses. For sufficiently deep cavities with vertical walls and close to liquid-gas phase coexistence in the bulk, the film thicknesses exhibit an effective planar scaling regime, which as function of undersaturation is characterized by a power law with the common critical exponent  $-1/3$  as for a flat substrate, but with the amplitude depending on the geometrical features.

PACS numbers: 68.08.Bc, 68.08.-p, 05.70.Np

## I. INTRODUCTION

It is well known that a non-planar topography of a substrate modifies its wetting properties significantly. Accordingly, experimental studies of complete wetting on substrates patterned by a two-dimensional lattice of nanopits [1], a one-dimensional array of wedges with finite depths [2], and arrays of microscopic nonlinear cusps or of semicircular channels [3] demonstrate the strong influence of nanocavities on the adsorption behavior relative to that on flat substrates. Theoretical studies of adsorption in infinitely deep [4] generalized wedges [5, 6] predict that such substrates modify the wetting exponents describing the divergence of the wetting film thickness upon approaching liquid-gas coexistence. Although nanopatterning of surfaces may result in drastic changes of their wettability, recent theoretical studies have revealed surprising hidden symmetries, or so-called covariances, which relate local adsorption properties for various different substrate geometries.

An example of such a geometrical covariance relating wedge and cone complete filling has been reported in Ref. [7]. It has been shown that the equilibrium midpoint interfacial heights  $l^{(0)}$  in a cone and a wedge obey the relation  $l_c^{(0)}(\Delta\mu, \alpha) = l_w^{(0)}(\Delta\mu/2, \alpha)$ , where  $\alpha$  is the substrate tilt angle and the undersaturation  $\Delta\mu \geq 0$  is the chemical potential deviation from bulk liquid-gas coexistence. This relation is valid for the leading asymptotic behaviors of  $l_{c,w}^{(0)}$  in the limit  $\Delta\mu \rightarrow 0^+$ .

In Ref. [8] we have demonstrated that complete wetting of substrates patterned by periodic arrays of grooves or quadratic lattices of pits (see Fig. 1) exhibits a geometrical covariance similar to the one described in Ref. [7]. Moreover, we have also identified a range of undersaturations, within which the midpoint interfacial height can be described by a *single* scaling function for all four types

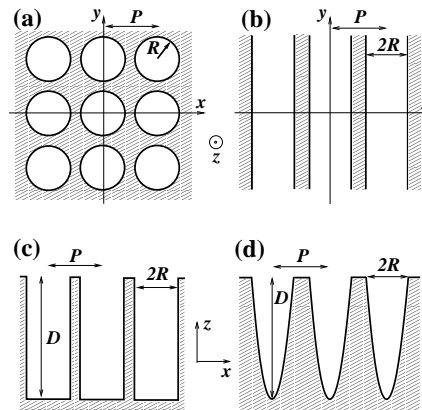


FIG. 1: (a), (b) Top views of the considered substrate geometries. (a) Quadratic lattice with lattice spacing  $P$  of identical, cylindrical or parabolic pits of radius  $R$ . (b) Periodic array of rectangular or parabolic grooves of width  $2R$ . (c), (d) Cross sections along the plane  $y = 0$  of arrays of rectangular grooves or cylindrical pits (c), and parabolic grooves or pits (d). All cavities have a finite depth  $D$ . The grooves have a macroscopic extension in the  $y$ -direction.

of substrate patterns. In this paper we extend the analyses of Ref. [8], showing inter alia that, in addition to the midpoint interfacial height, other parts of the interfacial profile exhibit the aforementioned covariance relation, too, while the laterally averaged interfacial profile does not.

Our analysis is based on an effective interface Hamiltonian approach [9, 10]. This approach has already been applied earlier to study wetting phenomena in a single groove [11], of a periodic array of grooves [12], in a wedge [4, 13], and also of chemically structured substrates [14, 15]. Although this approach does not model

the intrinsic structures of the emerging solid-liquid and of the depinning liquid-gas interfaces, it provides reliable results [10] concerning the growth and the morphology of wetting films, phase transitions, etc. It has been shown that the leading asymptotic behavior of the effective interface potential does not depend on the intrinsic structures of the emerging solid-liquid and liquid-gas interfaces and is given by the so-called sharp-kink approximation for the density distribution (see Sec. II) [10]. Therefore, this effective interface model is a reliable approach for complete wetting considered here, which probes the leading asymptotic behavior of the effective interface potential.

We consider rectangular or parabolic grooves and cylindrical or parabolic pits, taking into account the long range of both the substrate potential and the fluid-fluid interaction. The temperature  $T$  is chosen to be above the wetting transition temperature  $T_w$  of the unstructured planar substrate so that for  $\Delta\mu \rightarrow 0^+$  complete wetting occurs. (Similar considerations hold for binary liquid mixtures upon approaching their demixing transition from the mixed phase.) As function of undersaturation complete wetting of such substrates reveals four different scaling regimes [8]: filling, postfilling, effective planar, and planar, with the three crossover values between these four neighboring regimes denoted as  $\Delta\mu_{fil}^{p,g} > \Delta\mu_\pi^e > \Delta\mu_\pi > 0$ . Below we briefly describe all of them, providing also a short summary of the main results obtained. The aforementioned covariance relates the behavior of the midpoint wetting film thicknesses for all geometries and holds within an undersaturation range  $\Delta\mu_\pi^e \lesssim \Delta\mu \lesssim \Delta\mu_{fil}^{p,g}(R)$  (for  $\Delta\mu_\pi^e$  see below, the superscripts  $p, g$  refer to *pits* and *grooves*, respectively) which we call the *postfilling scaling regime*. In the case of cylindrical pits or rectangular grooves, for  $\Delta\mu \searrow \Delta\mu_{fil}^{p,g}(R)$  and for sufficiently large  $D/R$ , the analogue of capillary condensation occurs such that the pits or grooves are rapidly, but continuously, filled by the liquid. However, in the case of the parabolic pits and grooves,  $\Delta\mu_{fil}^{p,g}$  marks the crossover from the continuous power-law filling for  $\Delta\mu > \Delta\mu_{fil}^{p,g}$  to the postfilling scaling regime. We find numerically for  $R/\sigma \gtrsim 50$  (see Fig. 1), where  $\sigma$  is a molecular length scale,  $\Delta\mu_{fil}^{p,g}(R) \sim R^{-1-\delta}$  with a small positive effective exponent  $\delta$ , and  $\Delta\mu_{fil}^p = 2\Delta\mu_{fil}^g$ .

If we denote the equilibrium interface height at the position of the symmetry axes of the cylindrical or parabolic pits as  $l_p^{(0)}$ , and in the middle of the rectangular or parabolic grooves as  $l_g^{(0)}$ , we obtain in the postfilling regime

$$l_{p,g}^{(0)}(\Delta\mu, R, P, D) = R\Lambda_{p,g}\left(\frac{\Delta\mu}{\varepsilon_f}\left(\frac{R}{\sigma}\right)^{1+\delta}\right) \quad (1)$$

and

$$\Lambda_p(v) = \Lambda_g(v/2), \quad (2)$$

where  $\varepsilon_f$  is a molecular energy scale. Equation (2) expresses the same covariance relation as the one reported

in Ref. [7]. The dimensionless scaling functions  $\Lambda_{p,g}(x)$  of the postfilling regime do not depend on  $D$  or  $P$ , i.e., within this regime the midpoint interfacial heights increase upon decreasing undersaturation in the same way for an isolated cavity as for arrays of them.

For  $\Delta\mu < \Delta\mu_\pi^e$  the cavities are completely filled by the liquid and the equilibrium local interface heights  $l_{p,g}(x, y) = l_{p,g}$  become de facto independent of the lateral coordinates  $\mathbf{x} \equiv (x, y)$ . In the case of the rectangular grooves or cylindrical pits,  $\Delta\mu_\pi^e$  marks the crossover from the postfilling scaling regime to the *effective planar scaling regime* within which the wetting behavior of geometrically patterned substrates can be mapped onto that of layered, laterally homogeneous solids. The upper layer of those ersatz solids has a thickness  $D$  and its composition is related to the geometrical parameters  $R$  and  $P$ . This results in the following scaling relations for the effective planar scaling regime:

$$l_{p,g}(\Delta\mu, R, P, D) = (\Phi_{p,g})^{\frac{1}{3}}l_\pi(\Delta\mu),$$

$$\Phi_p \equiv 1 - \pi\left(\frac{R}{P}\right)^2, \quad \Phi_g \equiv 1 - \frac{2R}{P}, \quad (3)$$

where  $l_\pi$  is the thickness of the adsorbed liquid film on the corresponding original non-structured planar substrate.  $\Phi_p$  and  $\Phi_g$  are the areal fractions of solid in the top layer,  $z = 0$ , of substrates with cylindrical pit and rectangular groove patterns, respectively. For  $D \rightarrow 0$  the width of the effective planar regime, i.e., the range of applicability of Eq. 3 vanishes.

Finally, at  $\Delta\mu = \Delta\mu_\pi \sim D^{-3}$  with  $\Delta\mu_\pi < \Delta\mu_\pi^e$  the systems cross over to the *planar scaling* regime, in which the geometrical patterns are irrelevant. In the case of the parabolic pits and grooves, we do not observe the effective planar scaling regime. There is rather an extended crossover region from the postfilling scaling regime to the planar one.

In Sect. II we provide connections between microscopic density functional theory and the effective interface potential approach. In Sect. III we describe in detail the four scaling regimes, which are revealed by the midpoint interfacial heights as functions of undersaturation. Sect. IV provides a comparison with experimental data and Sect. V summarizes our main results and provides an outlook.

## II. EFFECTIVE INTERFACE HAMILTONIAN

We start from the following grand canonical density functional for inhomogeneous fluids characterized by the number density  $\rho(\mathbf{r})$  [16]:

$$\Omega[\{\rho(\mathbf{r})\}, T, \mu] = \int d^3r f_{HS}(\rho(\mathbf{r}), T)$$

$$+ \frac{1}{2} \int d^3r \int d^3r' w(|\mathbf{r} - \mathbf{r}'|) \rho(\mathbf{r}) \rho(\mathbf{r}')$$

$$+ \int d^3r (\rho_s V(\mathbf{r}) - \mu) \rho(\mathbf{r}). \quad (4)$$

The integrations are performed over the region accessible to the fluid;  $w(r)$  describes the long-ranged attractive part of the fluid-fluid interaction potential and decays at large distances  $\sim r^{-6}$ . The short-ranged repulsion is treated according to the Weeks-Chandler-Andersen (WCA) approximation [17] by introducing a reference system of hard spheres with bulk free energy density  $f_{HS}(\rho, T)$ ;  $\mu$  is the chemical potential and  $V(\mathbf{r})$  is the substrate potential, which can be obtained by integrating the fluid-substrate pair potential  $w_s(r)$  over the region occupied by the substrate particles with number density  $\rho_s$ . The equilibrium density distribution minimizes  $\Omega$ . In order to make analytic progress we seek the minimum of  $\Omega[\rho(\mathbf{r})]$  within the subspace of steplike varying density profiles [9, 10]:

$$\rho(\mathbf{r} = (\mathbf{x}, z)) = \Theta(z - s(\mathbf{x} = (x, y))) \times (\rho_l \Theta(l(\mathbf{x}) - z) + \rho_g \Theta(z - l(\mathbf{x}))), \quad (5)$$

where  $\rho_l$  and  $\rho_g$  are the number densities of the bulk liquid and gas phases, respectively;  $s(\mathbf{x})$  denotes the substrate surface which is in contact with the fluid;  $z = l(\mathbf{x})$  is the local position of the liquid-gas interface assuming the absence of bubbles and overhangs; and  $\Theta$  is the Heaviside step function. Inserting Eq. (5) into Eq. (4) yields the grand canonical potential  $\Omega$  as a functional of the interface morphology  $l(\mathbf{x})$ :

$$\Omega[\{l(\mathbf{x})\}; \rho_l, \rho_g, \mu] = \text{const} + \int_{\mathcal{A}} d^2x (\Delta\Omega l(\mathbf{x}) + \Sigma_{lg}(\mathbf{x}, l(\mathbf{x})) + W(\mathbf{x}, l(\mathbf{x}))). \quad (6)$$

$\mathcal{A}$  is a macroscopic area,  $\text{const}$  denotes the sum of all terms independent of  $l(\mathbf{x})$ , and  $\Delta\Omega$  is the difference of the grand canonical potential densities of the uniform bulk liquid and gas phases, i.e.,  $\Delta\Omega \equiv \Omega_b(\rho_l, T, \mu) - \Omega_b(\rho_g, T, \mu)$ . Close to the bulk liquid-gas coexistence line  $\mu = \mu_0(T)$  one has  $\Delta\Omega = \Delta\rho\Delta\mu + O(\Delta\mu^2)$ , with  $\Delta\mu = \mu_0(T) - \mu \leq 0$ , and  $\Delta\rho = \rho_l - \rho_g$ .  $\Sigma_{lg}(\mathbf{x}, l(\mathbf{x}))$  describes the cost in free energy to maintain a laterally inhomogeneous interface configuration relative to that for the flat reference configuration (see Ref. [18]):

$$\Sigma_{lg}(\mathbf{x}, l(\mathbf{x})) = -(\Delta\rho)^2 \int_{\mathcal{A}} d^2x' \int_0^\infty dz \int_0^{l(\mathbf{x})-l(\mathbf{x}')} dz' w(|\mathbf{r} - \mathbf{r}'|). \quad (7)$$

The functional form of the effective interface potential  $W(\mathbf{x}, l(\mathbf{x}))$  depends on the substrate shape as well as the fluid-fluid and the substrate-fluid interaction potentials:

$$W(\mathbf{x}, l(\mathbf{x})) = \Delta\rho \int_{\mathcal{A}} d^2x' \int_{l(\mathbf{x})-s(\mathbf{x}')}^\infty dz \int_z^\infty dz' \times (\rho_l w(\sqrt{(\mathbf{x} - \mathbf{x}')^2 + z'^2}) - \rho_s w_s(\sqrt{(\mathbf{x} - \mathbf{x}')^2 + z'^2})). \quad (8)$$

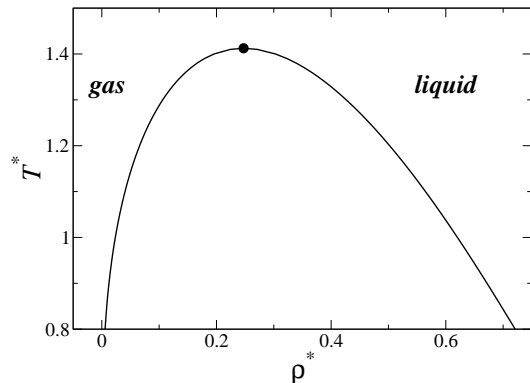


FIG. 2: Liquid-gas bulk phase diagram in terms of  $T^* = k_B T / \varepsilon_f$  and  $\rho^* = \rho \sigma^3$ . The critical point is given by  $(T_c^*, \rho_c^*) \approx (1.4124, 0.2473)$ .

The fluid particles are assumed to interact via a Lennard-Jones potential

$$\phi(r) = 4\varepsilon_f \left[ \left( \frac{\sigma}{r} \right)^{12} - \left( \frac{\sigma}{r} \right)^6 \right]. \quad (9)$$

We apply the WCA [17] procedure to split up the interaction into a repulsive part  $\phi_{rep}(r)$  and an attractive part  $\phi_{att}(r)$ , where

$$\phi_{rep}(r) = \begin{cases} \phi(r) + \varepsilon_f, & r < 2^{1/6}\sigma \\ 0, & r \geq 2^{1/6}\sigma \end{cases} \quad (10)$$

and

$$\phi_{att}(r) = \begin{cases} -\varepsilon_f, & r < 2^{1/6}\sigma \\ \phi(r), & r \geq 2^{1/6}\sigma. \end{cases} \quad (11)$$

The repulsive part gives rise to an effective, temperature dependent, hard sphere diameter

$$d(T) = \int_0^{2^{1/6}\sigma} dr \left[ 1 - \exp\left(-\frac{\phi_{rep}(r)}{k_B T}\right) \right]. \quad (12)$$

This expression is inserted into the Carnahan-Starling approximation for the free energy density of the hard-sphere fluid [19]

$$f_{HS}(\rho, T) = k_B T \rho \left( \ln(\rho \lambda^3) - 1 + \frac{4\eta - 3\eta^3}{(1 - \eta)^2} \right), \quad (13)$$

$$\eta = \frac{1}{6} \pi \rho d(T)^3,$$

where  $\lambda$  is the thermal de Broglie wavelength. The attractive part  $\phi_{att}(r)$  of the fluid-fluid interaction potential is approximated by

$$w(r) = w_0 \frac{4\sigma^3}{\pi^2} (\sigma^2 + r^2)^{-3}, \quad (14)$$

such that the integrated strength of  $w(r)$  equals that of the original  $\phi_{att}(r)$ :

$$w_0 = \int_{\mathbb{R}^3} d^3r w(r) = \int_{\mathbb{R}^3} d^3r \phi_{att}(r) = -\frac{32}{9}\sqrt{2}\pi\varepsilon_f\sigma^3. \quad (15)$$

Equation (14) resembles, but differs from the WCA expression  $\phi_{att}(r)$  for the attractive potential; this approximation offers the benefit to be able to perform certain integrations analytically. The actual values  $\rho_l$  and  $\rho_g$  minimize  $\Omega_b(\rho, T, \mu)$ , and the coexistence line  $\mu = \mu_0(T)$  is determined by the following equations:

$$\left. \frac{\partial \Omega_b}{\partial \rho} \right|_{\rho=\rho_l} = \left. \frac{\partial \Omega_b}{\partial \rho} \right|_{\rho=\rho_g} = 0 \quad (16)$$

and

$$\Omega_b(\rho_l) = \Omega_b(\rho_g). \quad (17)$$

The grand canonical potential density of the bulk system has the form

$$\Omega_b(\rho, T, \mu) = f_{HS}(\rho, T) + \frac{1}{2}w_0\rho^2 - \mu\rho. \quad (18)$$

The bulk phase diagram resulting from Eqs. (16)-(18) is shown in Fig. 2.

Since here we are only interested in complete wetting involving sufficiently thick films, the functional form in Eq. (14) can also be used to model the interaction potential between fluid and substrate particles, because under these circumstances only its asymptotic behavior at large distances matters:

$$w_s(r) = -\frac{128\sqrt{2}}{9\pi}\varepsilon_s\sigma_s^6(\sigma_s^2 + r^2)^{-3}. \quad (19)$$

In the following we use  $\sigma_s = \sigma$ . This leads to the following expression for the effective interface potential:

$$W(\mathbf{x}, l(\mathbf{x})) = A \times I_{V_s}(\mathbf{x}, l(\mathbf{x})),$$

$$I_{V_s}(\mathbf{x}, l(\mathbf{x})) = \int_{l(\mathbf{x})}^{\infty} dz \int_{V_s} d^3r' (\sigma^2 + |\mathbf{r} - \mathbf{r}'|^2)^{-3}, \quad (20)$$

where  $A = -\frac{128\sqrt{2}}{9\pi}\sigma^6\Delta\rho(\rho_l\varepsilon_f - \rho_s\varepsilon_s) > 0$  plays the role of an effective Hamaker constant, and  $V_s$  denotes the domain occupied by the substrate particles which are assumed to be homogeneously distributed within  $V_s$  with number density  $\rho_s$ . The effective interface potential of the planar substrate occupying the region  $z \leq 0$  is

$$W_\pi(l) = \frac{A\pi}{4\sigma^3} \left( \sigma - \frac{\pi l}{2} + l \arctan\left(\frac{l}{\sigma}\right) \right), \quad (21)$$

with  $W_\pi(l \gg \sigma) \approx A\pi/(12l^2)$  so that  $l_\pi(\Delta\mu \rightarrow 0) = (A\pi/(6\Delta\rho\Delta\mu))^{1/3}$ . By applying a small gradient expansion [18] for the nonlocal expression  $\Sigma_{l_g}(\mathbf{x}, l(\mathbf{x}))$  one

obtains the familiar local approximation for the grand canonical potential (see Eq. (6)):

$$\Omega^{loc}[\{l(\mathbf{x})\}; \rho_l, \rho_g, \mu] = \text{const} + \int d^2x \left( \sigma_{l_g} \sqrt{1 + (\nabla l)^2} + \Delta\mu\Delta\rho l + W(\mathbf{x}, l) \right); \quad (22)$$

$\sigma_{l_g}$  is the surface tension of the free liquid-vapor interface, which within the present sharp-kink approximation has the following form:

$$\sigma_{l_g} = -\frac{1}{2}(\Delta\rho)^2 \int_0^\infty dz \int_z^\infty dz' \int_{\mathcal{A}} d^2x w(\sqrt{\mathbf{x}^2 + z'^2}) = \frac{16\sqrt{2}(\Delta\rho\sigma^3)^2\varepsilon_f}{9\sigma^2}. \quad (23)$$

Having determined the bulk coexistence curve  $\mu_0(T)$ , in the following we minimize the functional in Eq. (22) numerically which yields the equilibrium interface height  $l(\mathbf{x})$  within mean-field approximation. The bulk liquid and gas densities  $\rho_l$  and  $\rho_g$ , respectively, are evaluated at coexistence, i.e.,  $\rho_l = \rho_l(T, \mu_0(T))$  and  $\rho_g = \rho_g(T, \mu_0(T))$ . All results presented below are obtained for  $T/T_c = 0.85$ . For the substrate structured with grooves the four integrals in the Eq. (20) can be calculated analytically, while for the two-dimensional lattices of cylindrical or parabolic pits only three of them can be carried out analytically. Whereas the capillary wave spectrum of  $\Omega$  given by Eq. (6) differs qualitatively [18, 20] from that of the local approximation in Eq. (22), the morphology of the wetting film is captured reliably by Eq. (22) apart from regions of high curvature [21] which do not play an important role in the present context. Therefore, it is legitimate to apply Eq. (22) even in the presence of long-ranged fluid-fluid interactions, which are additionally encoded in  $W(\mathbf{x}, l)$ .

### III. NUMERICAL RESULTS

For grooves, in Fig. 3 typical interfacial profiles  $l_g(x)$  are shown as obtained for several values of  $\Delta\mu$ . We are primarily concerned with the behavior of the midpoint heights  $l_{p,g}^{(0)}$  as functions of the undersaturation  $\Delta\mu$ . For all substrate geometries the midpoint heights  $l_{p,g}^{(0)}(\Delta\mu)$  exhibit four different regimes.

#### A. Large $\Delta\mu$ : filling and postfilling regimes

The first regime corresponds to the filling of the cavities. Cavities with vertical walls (rectangular grooves or cylindrical pits) are filled in a qualitatively different way compared to parabolic ones. For the case of cylindrical pits and rectangular grooves and for  $D/R$  large

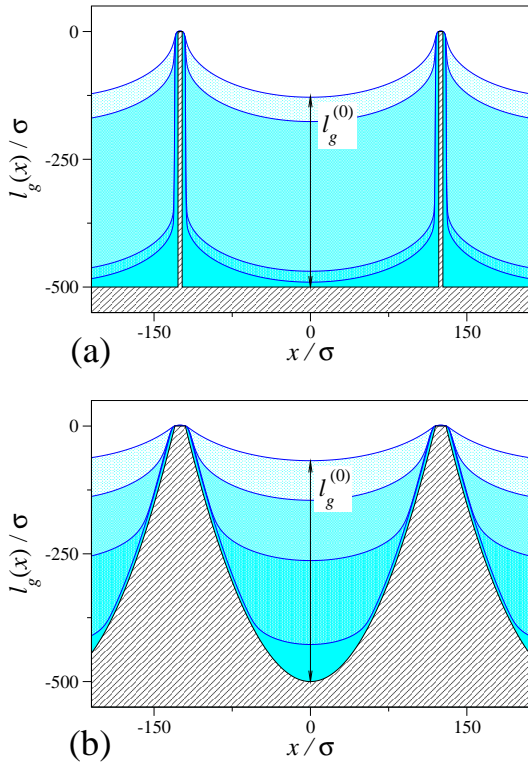


FIG. 3: Interfacial profiles  $l_g(x)$  (a) for rectangular grooves (which are translationally invariant in the  $y$  direction) and four values of undersaturation (top to bottom):  $\Delta\mu/\varepsilon_f = 0.00921, 0.00928, 0.00929, 0.0939$  which are close to  $\Delta\mu_{fil}^g$ ,  $R/\sigma = 123$ ; (b) for parabolic grooves for  $\Delta\mu/\varepsilon_f = 0.008, 0.01, 0.012, 0.02$  (top to bottom),  $R/\sigma = 120$ . For both structures  $P/\sigma = 250$  and  $D/\sigma = 500$  (see Fig. 1).  $l = 0$  corresponds to the top of the substrate structure at  $z = 0$ . Here the effective Hamaker constant is  $A/\varepsilon_f \approx 0.330$ , and the surface tension of the free liquid-gas interface is  $\sigma_{lg}\sigma^2/\varepsilon_f \approx 0.478$ .

enough, there exists a well defined value of the undersaturation  $\Delta\mu = \Delta\mu_{fil}^{p,g}$  at which an abrupt, but still continuous, filling of the cavities takes place. A similar behavior has been reported earlier for an isolated rectangular groove [11]. The filling of the vertical cavities is shown in Fig. 4(a), where  $l_{p,g}^{(0)}(\Delta\mu)$  are shown for several values of  $R$  and  $P$ . The interfacial profiles, which are shown in Fig. 3(a), are calculated for undersaturations close to  $\Delta\mu_{fil}^g$ ,  $|\Delta\mu - \Delta\mu_{fil}^g| < 0.002$ , and  $R/\sigma = 123$ .  $\Delta\mu_{fil}^{p,g}$  depend only on the lateral size  $R$  of the cavities, but not on the depth  $D$ . We find numerically that  $\Delta\mu_{fil}^{p,g} \sim R^{-1-\delta}$ , with an effective exponent  $\delta \approx 0.035$  for both the cylindrical pits and the rectangular grooves.

Different from the previous case, the complete filling of the parabolic cavities is described by an effective power law,  $l_{p,g}^{(0)}(\Delta\mu, R, D) \sim \Delta\mu^{-\gamma(R,D)}$ , which is valid for  $\Delta\mu \gtrsim \Delta\mu_{fil}^{p,g}$  only (see Fig. 5(a)). The effective exponent  $\gamma$  ranges from ca. 3.1, for  $R = 245\sigma$ , to ca. 2.0, for  $R = 50\sigma$ , at a cavity depth  $D = 500\sigma$ . The value  $\gamma = 2$  is expected to hold for an infinitely deep, single

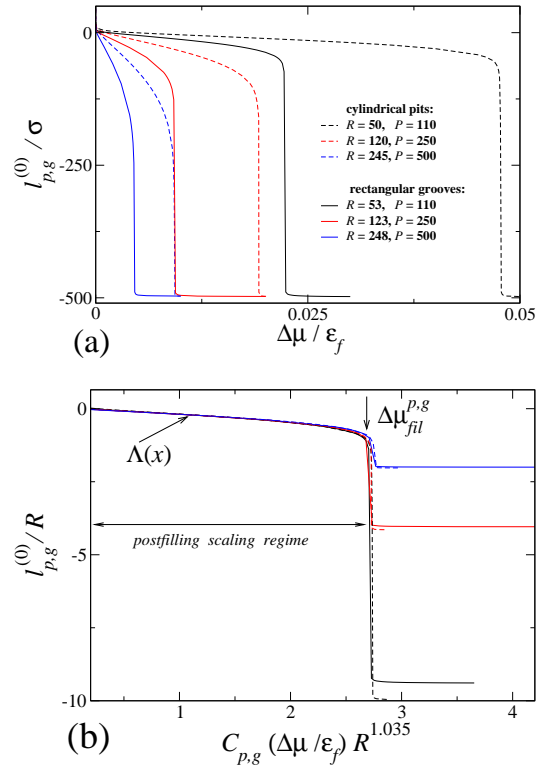


FIG. 4: (a) Interfacial heights (measured from the top substrate layer at  $z = 0$ ) at the middle of the cylindrical pits,  $l_p^{(0)}$  (dashed lines), and of the rectangular grooves,  $l_g^{(0)}$  (solid lines), as a function of undersaturation  $\Delta\mu$  measured in units of the energy scale  $\varepsilon_f$  of the fluid-fluid interaction. (b) Rescaling the variables according to Eqs. (1) and (2) leads to data collapse in the postfilling scaling regime;  $C_p = 1$  and  $C_g = 2$ . The depth of the cavities is  $D = 500$ . All lengths are measured in units of  $\sigma$ .  $A/\varepsilon_f \approx 0.330$ , and  $\sigma_{lg}\sigma^2/\varepsilon_f \approx 0.478$ .  $\Lambda(x)$  denotes the scaling function introduced in Eq. (2).

parabolic wedge [5]. For both vertical and parabolic cavities, the complete filling obeys the covariance relation  $l_p^{(0)}(\Delta\mu, R, D) = l_g^{(0)}(\Delta\mu/2, R, D)$  valid for  $\Delta\mu \gtrsim \Delta\mu_{fil}^{p,g}$ .

For  $\Delta\mu < \Delta\mu_{fil}^{p,g}$  the midpoint height for all patterns shows an almost linear dependence on  $\Delta\mu$  on normal scales. The interfacial profiles still reflect the geometrical patterns, i.e., there are considerable lateral variations of the interfacial heights. For large enough  $D$  there exists a range of undersaturations ( $\Delta\mu_{\pi}^e, \Delta\mu_{fil}^{p,g}$ ) within which the midpoint interfacial height for all four substrate geometries can be described by a *single* scaling function [8]. We call this range of  $\Delta\mu$  the postfilling scaling regime. The lower bound  $\Delta\mu_{\pi}^e$  of this regime is a decreasing function of the cavities size  $R$ . We find that for  $\Delta\mu \in (\Delta\mu_{\pi}^e, \Delta\mu_{fil}^{p,g})$  the slopes of the  $l_{p,g}^{(0)}$  curves scale as  $R^\alpha$  with  $\alpha \approx 2$ . Combining this result with the scaling of the chemical potential  $\Delta\mu_{fil}^{p,g}$  at the crossover to the filling scaling regime, we propose for the functions  $l_{p,g}^{(0)}$  in the postfilling regime the scaling forms given by Eq. (1).

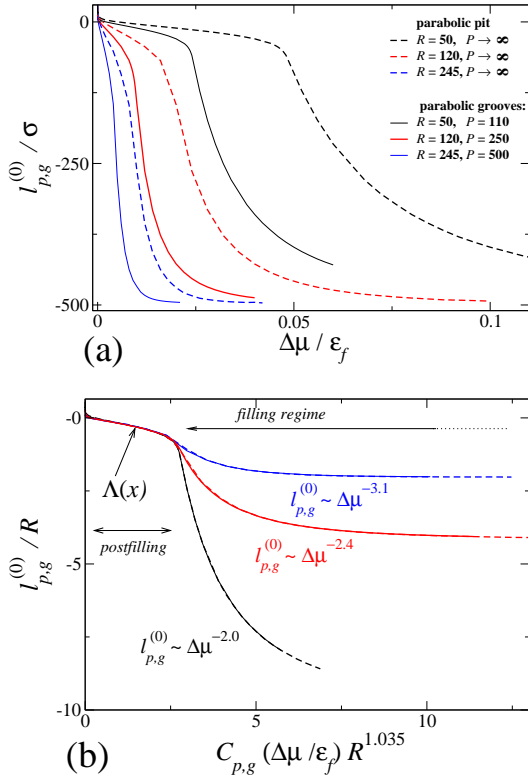


FIG. 5: (a) Interfacial heights at the middle of the parabolic pit,  $l_p^{(0)}$  (dashed lines), and of the parabolic grooves,  $l_g^{(0)}$  (solid lines), as a function of  $\Delta\mu$ . (b) Rescaling the variables according to Eqs. (1) and (2) leads to data collapse for  $\Delta\mu \in (\Delta\mu_\pi^e, \Delta\mu_{fil}^{p,g})$ ;  $C_p = 1$  and  $C_g = 2$ . The depth of the cavities is  $D = 500$ . All length are measured in units of  $\sigma$ .  $A/\varepsilon_f \approx 0.330$ , and  $\sigma_{lg}\sigma^2/\varepsilon_f \approx 0.478$ .  $\Lambda(x)$  denotes the scaling function introduced in Eq. (2). The filling regime ends at large  $\Delta\mu$  (dotted line) where the wetting films in the center become microscopically thin so that scaling breaks down.

In this postfilling scaling regime the scaling function  $\Lambda_g$  describes rectangular as well as parabolic grooves, and similarly  $\Lambda_p$  describes cylindrical and parabolic pits. The scaling functions  $\Lambda_{p,g}$  and the corresponding data collapse upon suitably rescaling the chemical potential and the midpoint heights are shown in Figs. 4(b) and 5(b) for the case of vertical and parabolic cavities, respectively. In accordance with Eq. 2 the difference between  $\Lambda_p(x)$  and  $\Lambda_g(x)$  can be absorbed in the rescaling factors  $C_p = 1$  and  $C_g = 2$ . Inspection tells that the resulting common scaling function denoted as  $\Lambda(x)$  in Figs. 4(b) and 5(b) are indeed identical. The scaling functions  $\Lambda_{p,g}$  in the postfilling scaling regime do not depend on the cavity depth  $D$  which is demonstrated in Fig. 6, where  $l_p^{(0)}(\Delta\mu)$  is shown in the case of cylindrical pits and for several values of  $D$ . For even smaller values of  $D/R$ , owing to the finite-size rounding effects, the filling of the cavities does not occur at a certain value of the chemical potential, but there is an entire transition region. As a result, the range of the postfilling scaling regime shrinks

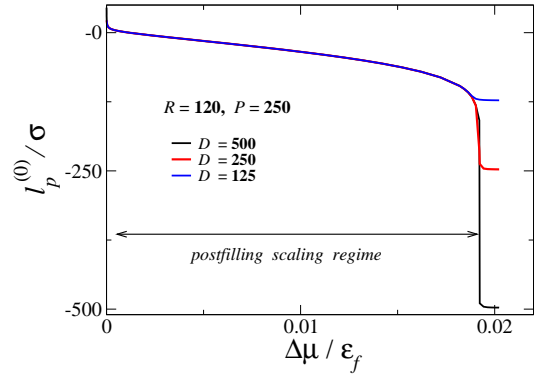


FIG. 6: Interfacial heights  $l_p^{(0)}$  in the middle of the cylindrical pits as a function of undersaturation  $\Delta\mu$  for several values of the pit depth  $D$  (see Fig. 1). All lengths are measured in units of  $\sigma$ ;  $A/\varepsilon_f \approx 0.330$  and  $\sigma_{lg}\sigma^2/\varepsilon_f \approx 0.478$ .

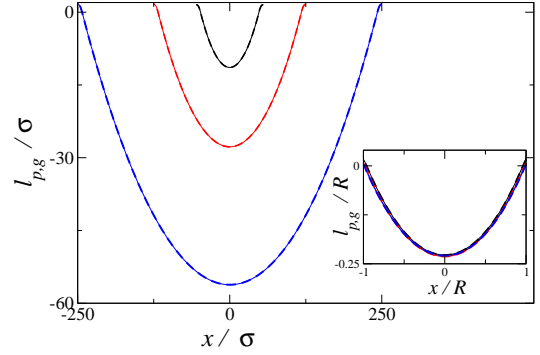


FIG. 7: Interfacial profiles within the cavity regions for cylindrical pits,  $l_p(x, y = 0)$  (dashed lines), and rectangular grooves,  $l_g(x)$  (full lines), for the postfilling scaling regime. Black, red, and blue colors correspond to  $(R = 50, P = 110)$ ,  $(R = 120, P = 250)$ , and  $(R = 245, P = 500)$ , respectively. The dashed and full interfacial profiles are calculated for two different values of the undersaturation which both satisfy  $C_{p,g}\Delta\mu/\varepsilon_f(R/\sigma)^{1.035} = 1.18$  with  $C_p = 1$  and  $C_g = 2$ , respectively. In the inset the axes are rescaled by  $R^{-1}$  leading to complete data collapse.  $D = 500$  and  $\sigma$  is the length unit;  $A/\varepsilon_f \approx 0.330$  and  $\sigma_{lg}\sigma^2/\varepsilon_f \approx 0.478$ .

as  $D/R$  decreases.  $\Lambda_{p,g}$  do not depend on the pattern periodicity  $P$  either. In the case of a single cavity, i.e., in the limit  $P \rightarrow \infty$ , we obtain the same curves  $l_{p,g}^{(0)}(\Delta\mu)$  as those presented in Figs. 4 and 5. Furthermore, we find that for the filling and postfilling scaling regimes not only  $l_{p,g}^{(0)}$ , but also the full interfacial profiles  $l_{p,g}(\mathbf{x})$  are, within numerical accuracy, independent of the pattern periodicities  $P$  studied here. This implies that for the case of pits (both cylindrical and parabolic) the interfacial profile within the cavity region is, to a good approximation, rotational symmetric around the symmetry axis of the pit, i.e.,  $l_p(\mathbf{x}) = l_p(r_p)$ , where  $r_p \lesssim R$  is the radial distance from the symmetry axis of a pit.

In the postfilling scaling regime, in addition to the

midpoint interfacial heights, those values of the profiles  $l_{p,g}(\mathbf{x})$ , which are taken off center at the same distance  $r_{p,g}/R \lesssim 1$  from the symmetry axis of a pit or from the midplane of a groove, also satisfy generalized scaling relations similar to Eqs. (1) and (2):

$$l_p(\mathbf{x}, \Delta\mu, R, P, D) = R\Lambda_p\left(\frac{r_p}{R}, \frac{\Delta\mu}{\varepsilon_f}\left(\frac{R}{\sigma}\right)^{1+\delta}\right) \quad (24)$$

$$l_g(x, \Delta\mu, R, P, D) = R\Lambda_g\left(\frac{r_g}{R}, \frac{\Delta\mu}{\varepsilon_f}\left(\frac{R}{\sigma}\right)^{1+\delta}\right), \quad (25)$$

where  $r_p = \sqrt{(x-x_0)^2 + (y-y_0)^2}$  is the radial distance from the symmetry axis of a pit at  $(x, y) = (x_0, y_0)$ ;  $r_g = |x-x_0|$  is the distance from the midplane of a groove at  $x = x_0$ . The scaling functions  $\Lambda_p$  and  $\Lambda_g$  obey the covariance relation

$$\Lambda_p(u, v) = \Lambda_g(u, v/2), \quad u \lesssim 1. \quad (26)$$

The interfacial profiles for cylindrical pits,  $l_p$ , and rectangular grooves,  $l_g$ , are shown in the Fig. 7 for several  $R$ . The profiles are calculate for two different undersaturations  $\Delta\mu$  within the postfilling regime which both satisfy  $C_{p,g}\Delta\mu/\varepsilon_f(R/\sigma)^{1.035} = 1.18$  with  $C_p = 1$  and  $C_g = 2$ , respectively. Rescaling the variables according to Eq. (25) leads to data collapse. Equation (26) means that, for fixed  $R$  and certain values of undersaturation, the interfacial profile within a pit region can be considered as a surface of revolution generated by the function  $l_g(r_g)$  which characterizes the interfacial profile within a groove region. This also holds within the filling scaling regime.

We also consider the lateral average  $\bar{l}_{p,g} = \int d^2x l_{p,g}(\mathbf{x})/\bar{\mathcal{A}}$  of the interfacial profiles  $l_{p,g}(\mathbf{x})$  with the integral running over the lateral surface area  $\bar{\mathcal{A}}$  of a unit cell of the surface pattern. This quantity is related to the excess adsorption  $\Gamma = \int d^3r(\rho(\mathbf{r}) - \rho_b)/\bar{\mathcal{A}}$  per area of the cell, with the integral running over the region accessible to the fluid above a unit cell. Using the sharp-kink approximation for the density (see Eq. (5))  $\Gamma$  can be expressed as

$$\begin{aligned} \Gamma_{p,g} &= \frac{1}{\bar{\mathcal{A}}}\Delta\rho \int_{\bar{\mathcal{A}}} d^2x (l(\mathbf{x}) - s(\mathbf{x})) \\ &= \Delta\rho \left( \bar{l}_{p,g} + \frac{V_{p,g}}{\bar{\mathcal{A}}} \right), \end{aligned} \quad (27)$$

where  $V_{p,g}$  is the volume of a pit or groove, respectively. For rectangular grooves and cylindrical pits Fig. 8 shows the corresponding results for  $\bar{l}_{p,g}(\Delta\mu)$  with the chemical potential and  $\bar{l}$  rescaled according to Eqs. (1) and (2). The laterally averaged interfacial profile in the postfilling scaling regime also obeys the scaling described by Eq. (1), but the scaling functions for the rectangular grooves and the cylindrical pits do *not* satisfy the covariance relation given by Eq. (2). The same result holds for the case of parabolic pits and grooves, which is shown in Fig. 9. Moreover, the scaling functions which are shown

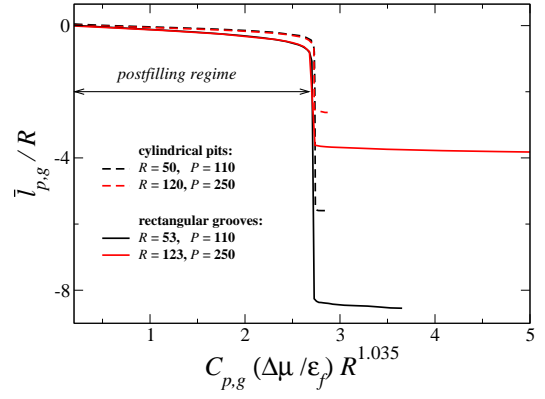


FIG. 8: Rescaled laterally averaged interfacial profile for cylindrical pits,  $\bar{l}_p$  (dashed lines), and for rectangular grooves,  $\bar{l}_g$  (full lines), as a function of undersaturation  $\Delta\mu$ . The rescaling of the variables according to Eqs. (1) and (2) leads to two different scaling curves describing the cylindrical pits and the rectangular grooves, respectively. Thus the covariance relation given by Eq. (2) is not fulfilled. Compare Fig. 4(b) which shows that the postfilling scaling functions for the midpoint interfacial height are the same for these two cavity types.  $C_p = 1$  and  $C_g = 2$ ,  $D = 500$ , and  $\sigma$  is the length unit;  $A/\varepsilon_f \approx 0.330$  and  $\sigma_{lg}\sigma^2/\varepsilon_f \approx 0.478$ .

in Fig. 8, describe also the laterally averaged interfacial profiles for parabolic pits and grooves, respectively. Geometrical considerations show that the lateral average of a troughlike surface generated by a function of a single variable is smaller than the lateral average of the corresponding rotationally symmetric surface generated by revolving the same function around the symmetry axis. As shown above, both surfaces obey the covariance scaling properties. Therefore this inequality of the lateral averages implies that this covariance does not hold for the lateral averages.

### B. Small $\Delta\mu$ : effective planar and planar scaling regimes

For undersaturations below a certain value  $\Delta\mu_\pi^e$ , i.e., closer to gas-liquid coexistence, the liquid-gas interface becomes flat (Fig. 10), its height denoted as  $l_{p,g}$  for the pit and groove patterns, respectively. For these flat wetting films the functional in Eq. (22) reduces to a function of a single variable  $l_{p,g}$  the minimum of which determines the equilibrium thicknesses of the wetting films in this regime. The corresponding results  $l_{p,g}(\Delta\mu)$  for cylindrical pits and rectangular grooves are presented in Fig. 11 and Fig. 12, respectively. For these two substrate geometries there is an interval of undersaturations  $(\Delta\mu_\pi, \Delta\mu_\pi^e)$ , within which both  $l_p$  and  $l_g$  reveal the same power law growth  $l_{p,g} \sim \Delta\mu^{-1/3}$  as for a flat surface, but with different amplitudes reflecting different, geometry dependent, effective Hamaker constants  $A^e$ . We call this range of un-



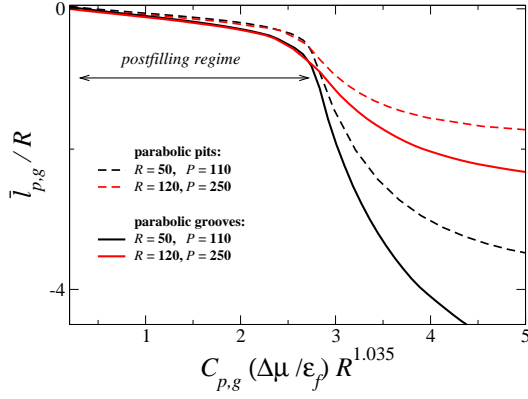


FIG. 9: Rescaled laterally averaged interfacial profile for parabolic pits,  $\bar{l}_p$  (dashed lines), and grooves,  $\bar{l}_g$  (full lines), as a function of undersaturation  $\Delta\mu$ . The rescaling of the variables according to Eqs. (1) and (2) leads to two different scaling curves describing the cylindrical pits and the rectangular grooves, respectively. Compare Fig. 5(b) which shows that the postfilling scaling functions for the midpoint interfacial height are the same for these two cavity types.  $C_p = 1$  and  $C_g = 2$ ,  $D = 500$ , and  $\sigma$  is the length unit;  $A/\varepsilon_f \approx 0.330$  and  $\sigma_{lg}\sigma^2/\varepsilon_f \approx 0.478$ .

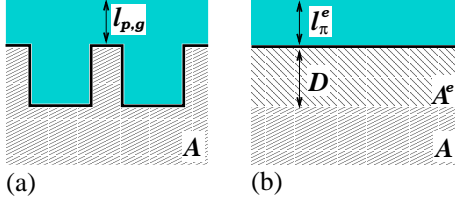


FIG. 10: (a) Schematically drawn liquid wetting film morphology on substrates sculptured by cylindrical pits or rectangular grooves within the effective planar scaling regime. (b) Wetting film of thickness  $l_\pi^e$  on a flat layered solid. The top layer has a thickness  $D$  with an effective Hamaker constant  $A^e$  whereas the semi-infinite bottom part of the substrate is characterized by the Hamaker constant  $A$ .

undersaturation the effective planar scaling regime. Within this regime the substrates sculptured by cavities with vertical walls are equivalent to layered and flat ersatz solids (see Fig. 10(b)) with the effective interface potential [12]

$$W(l \gg \sigma) \approx \frac{\pi}{12} \left( \frac{A}{(l+D)^2} + \frac{A^e}{l^2} - \frac{A^e}{(l+D)^2} \right). \quad (28)$$

Here the first term corresponds to a flat semi-infinite,  $z \in (-\infty, -D)$ , solid with Hamaker constant  $A$  and the second and the third are the corrections due to the finite slab,  $z \in (-D, 0)$ , with effective Hamaker constant  $A^e$ . For  $\sigma \ll l \lesssim D$ , it is a good approximation to ignore the bottom part of the substrate (i.e., the first and the third terms in  $W(l \gg \sigma)$ ) so that the amplitude is determined by the effective Hamaker constant  $A^e$ .

With  $\Lambda_s$  we denote that region of the sculptured part

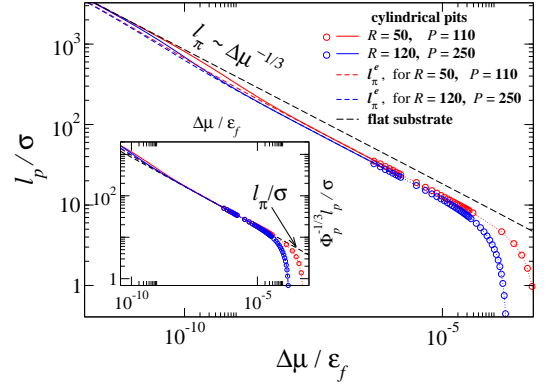


FIG. 11: Wetting film thickness  $l_p$  above cylindrical pits for small  $\Delta\mu$ . The solid lines are obtained by minimizing Eq. (22) in the subspace of laterally constant interfacial heights  $l(\mathbf{x}) = l_p$ . The circles represent the mid-point interfacial heights  $l_p^{(0)}$  and are the results of the full numerical minimization of the Hamiltonian in Eq. (22). The circles are plotted in that  $\Delta\mu$  range for which the deviations from the full and dashed lines become detectable. The dashed lines correspond to the film thicknesses  $l_\pi^e(\Delta\mu)$  on layered flat ersatz substrates (see Fig. 10), with a top layer of height  $D$  and an effective Hamaker constant  $A^e = A\Phi_p \equiv A(1 - \pi(R/P)^2)$ , where  $A$  is the Hamaker constant of the solid without pits. In the inset the vertical axis is rescaled according to the scaling relation given in Eq. (3) leading to data collapse and – after rescaling – agreement with  $l_\pi$  within an intermediate regime,  $\Delta\mu_\pi < \Delta\mu < \Delta\mu_\pi^e$ , the width of which increases as  $\Delta\mu_\pi^e - \text{const} \times D^{-3}$  for  $D \rightarrow \infty$ . The pit depth is  $D = 500\sigma$ ;  $A/\varepsilon_f \approx 0.330$  and  $\sigma_{lg}\sigma^2/\varepsilon_f \approx 0.478$ .

of the substrate ( $z \in [-D, 0]$ ), which is occupied by the solid, and with  $\Lambda_0$  the entire slab  $z \in [-D, 0]$ . The equivalence of the patterned and the flat layered substrate actually means  $W_{\Lambda_s}(\mathbf{x}, l) = W_{\Lambda_0}(\mathbf{x}, l)$ . With Eq. (20) one obtains  $A^e = A I_{\Lambda_s} / I_{\Lambda_0}$ . For  $l \gg \sigma$  the integrals  $I_{\Lambda_i}$  ( $i = s, 0$ ) can be approximated as

$$I_{\Lambda_i} \approx \int_l^\infty dz \int_{\Lambda_i} \frac{d^3 r'}{(z-z')^6} \left( 1 - 3 \frac{\sigma^2 + \|\mathbf{x} - \mathbf{x}'\|^2}{(z-z')^2} \right). \quad (29)$$

Actually,  $I_{\Lambda_s}$  is a function of  $\mathbf{x}$ , which varies across a unit cell and only its leading term  $\sim l^{-2}$  is laterally constant. In Eq. (29) taking into account only the leading term as function of  $l$  one finds  $A^e \approx AS_s/S_0$ , where  $S_s/S_0$  is the fraction of area occupied by the solid in the top layer of the substrates patterned by cavities with vertical walls. Thus, one has  $A_g^e \approx A\Phi_g$  for the rectangular grooves and  $A_p^e \approx A\Phi_p$  for cylindrical pits (see Eq. (3)). The thicknesses  $l_\pi^e(\Delta\mu)$  of the wetting films on such layered ersatz substrates, which effectively correspond to arrays of grooves, are almost indistinguishable from the corresponding actual ones  $l_g$ . For lattices of cylindrical pits in Fig. 11 we present  $l_\pi^e(\Delta\mu)$  (dashed lines) on layered substrates, and find agreement with the actual thicknesses  $l_p(\Delta\mu)$  within the effective planar scaling regime. There-



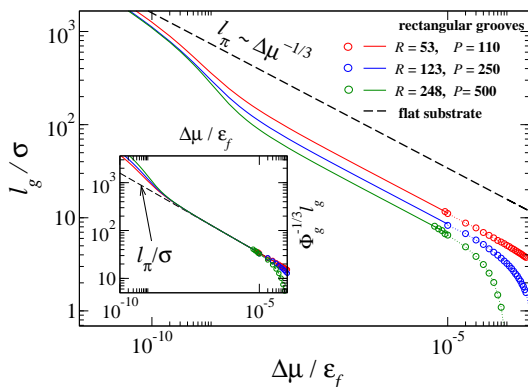


FIG. 12: Wetting film thickness  $l_g$  above rectangular groove patterns for small  $\Delta\mu$ . The solid lines are obtained by minimizing Eq. (22) in the subspace of laterally constant interfacial heights  $l(\mathbf{x}) = l_g$ . The circles represent the mid-point interfacial heights  $l_g^{(0)}$  and are the results of the full numerical minimization of the Hamiltonian in Eq. (22). The circles are plotted in that  $\Delta\mu$  range for which the deviations from the full and dashed lines become detectable. On the present scales the data for  $l_g$  are indistinguishable from the lines  $l_\pi^e(\Delta\mu)$  obtained for layered flat ersatz substrates with a top layer of height  $D$  and an effective Hamaker constant  $A^e = A\Phi_g \equiv A(1 - 2R/P)$ , where  $A$  is the Hamaker constant of the solid without grooves. In the inset the vertical axis is rescaled according to the scaling relation given in Eq. (3) leading to data collapse and – after rescaling – agreement with  $l_\pi$  within an intermediate regime,  $\Delta\mu_\pi < \Delta\mu < \Delta\mu_\pi^e$ , the width of which increases as  $\Delta\mu_\pi^e - \text{const} \times D^{-3}$  for  $D \rightarrow \infty$ . The groove depth is  $D = 500\sigma$ ;  $A/\epsilon_f \approx 0.330$  and  $\sigma l_g \sigma^2 / \epsilon_f \approx 0.478$ .

fore we can conclude that for sufficiently thick wetting films  $l_{p,g}$  obey the scaling relation given in Eq. (3). Indeed, after rescaling the film thicknesses by the geometry-dependent factors  $(\Phi_{p,g})^{-1/3}$ , the curves for  $l_{p,g}$  collapse and, within the numerical precision, they coincide with the curve for  $l_\pi$ . This is shown in the insets of Figs. 11 and 12. In the case of parabolic cavities we have found numerically that the corresponding curves for  $l_{p,g}$  do not reveal this effective planar scaling regime, but gradually cross over to the planar one, denoted as  $l_\pi$  [8]. We emphasize that the effective planar regime exists *only* for patterns with *vertical* walls. Thus, we also expect this regime to exist for lattices of cylindrical nanoposts, but not for, e.g., sawlike substrate surfaces or periodic arrays of trapezoidal cavities.

As  $l_{p,g}$  reach the value  $\sim D$ , i.e., at  $\Delta\mu = \Delta\mu_\pi \sim D^{-3}$ , a crossover to the planar scaling regime takes place. In the planar scaling regime  $\Delta\mu \lesssim \Delta\mu_\pi$  the geometrical patterns have become irrelevant. Thus the range of applicability  $\Delta\mu_\pi^e - \Delta\mu_\pi$  of Eq. 3 increases with the cavity depth  $D$  as  $\Delta\mu_\pi^e - \text{const} \times D^{-3}$ , whereas for  $D \rightarrow 0$   $\Delta\mu_\pi$  merges with  $\Delta\mu_\pi^e$ , eliminating the effective planar scaling regime.

#### IV. COMPARISON WITH EXPERIMENTAL DATA

In this section we compare our results with the corresponding experimental data of Ref. [1], where the adsorption of methylcyclohexane (MCH) on a nanopatterned silicon substrate has been studied using X-ray reflectivity (XR) and grazing incident diffraction (GID) techniques. The substrate was patterned by a hexagonal lattice of parabolic pits with radius  $R \approx 123\text{\AA}$ , depth  $D \approx 200\text{\AA}$ , and lattice constant  $P \approx 394\text{\AA}$ . Accordingly, in the following the theoretical data have been obtained for a hexagonal pattern, too. The data in Ref. [1] have been interpreted in terms of the excess adsorption  $\Gamma = \Gamma_{in} + \Gamma_{out}$  as the sum of the excess adsorption  $\Gamma_{in}$  in the pit and the excess adsorption  $\Gamma_{out}$  above the pit opening (see inset in Fig. 13(a)). These two quantities are defined as

$$\Gamma_{in} = \frac{1}{\bar{A}} \int d^2x \int_{s(\mathbf{x})}^0 dz (\rho(\mathbf{r}) - \rho_g) \quad (30)$$

and

$$\Gamma_{out} = \frac{1}{\bar{A}} \int d^2x \int_0^\infty dz (\rho(\mathbf{r}) - \rho_g). \quad (31)$$

Using the sharp-kink approximation for the density profile (see Eq. (5)) Eqs. (30) and (31) take the form

$$\Gamma_{in} = \frac{\Delta\rho}{\bar{A}} \int d^2x (\Theta(-l(\mathbf{x}))l(\mathbf{x}) - s(\mathbf{x})), \quad (32)$$

and

$$\Gamma_{out} = \frac{\Delta\rho}{\bar{A}} \int d^2x \Theta(l(\mathbf{x}))l(\mathbf{x}). \quad (33)$$

In these experiments the thermodynamic deviation from liquid-vapor coexistence of MCH has been tuned via controlling a temperature difference  $\Delta T$  between the substrate and the reservoir of bulk liquid.  $\Delta T$  is related to the undersaturation  $\Delta\mu$  according to [1]  $\Delta T = \Delta\mu T/H$ , where  $T = 305\text{K}$  is the reservoir temperature, and  $H = 5.8 \times 10^{-20}\text{J}$  is the latent heat of vaporization per MCH molecule [1]. We have modeled MCH by a Lennard-Jones interaction potential with the parameters  $\sigma = 5.511\text{\AA}$  and  $\epsilon_f/k_B = 446\text{K}$  [22], which leads to  $\Delta T \approx 32.37 \frac{\Delta\mu}{\epsilon_f} \text{K}$ . By fitting the experimental reference data for the wetting film thickness on the corresponding planar substrate [1] to the expression  $l_\pi(\Delta\mu \rightarrow 0)$  given just below Eq. (21) we are able to determine the ratio  $A/(\epsilon_f \Delta\rho^*) \approx 1.006$  involving the Hamaker constant  $A$ . The last material parameter required to facilitate a quantitative comparison between our theory and the experimental data in Ref. [1] is the liquid-vapor surface tension

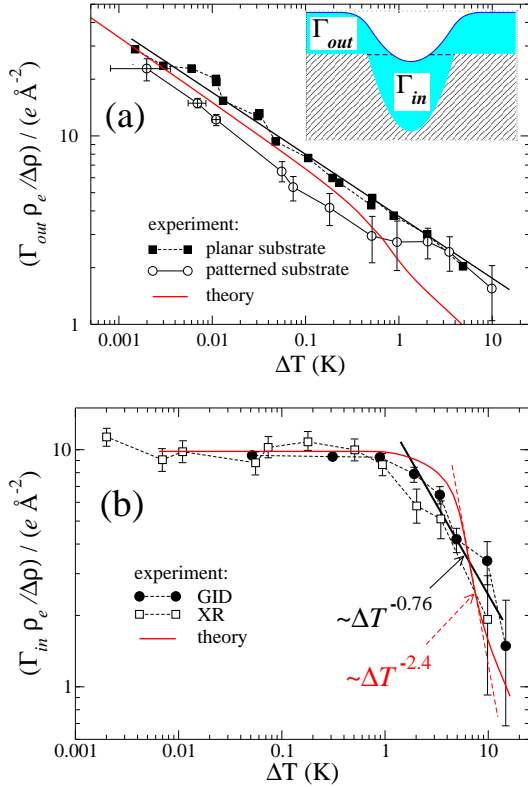


FIG. 13: Excess adsorptions (a)  $\Gamma_{out}(\Delta T)$  above the top of the substrate and (b)  $\Gamma_{in}(\Delta T)$  within the parabolic pits. Symbols and black lines denote experimental data from Ref. [1]. Red lines are the corresponding theoretical results (see main text).  $\rho_e = 0.26e/\text{\AA}^3$  is the electron density of the bulk MCH.  $\Delta T$  is proportional to  $\Delta\mu$ .

of MCH, for which we use  $\sigma_{lg} = 22.72 \frac{\text{dyn}}{\text{cm}}$  for  $T = 30^\circ\text{C}$  [23]. Using the values of  $\sigma$  and  $\varepsilon_f$  given above for MCH, we find  $\sigma_{lg}\sigma^2/\varepsilon_f \approx 1.149$ . According to Eq. (23) this value of the surface tension corresponds to  $\Delta\rho^* \approx 0.668$  or  $T^* \approx 0.88$  as follows from the bulk phase digram shown in Fig. 2. It is satisfactory to see that this value of the reduced temperature  $T^*/T_c^* = T/T_c \approx 0.88/1.41 \approx 0.62$  turns out to be reasonably close to the actual experimental ratio  $T/T_c = 305/572 \approx 0.53$ . With this there are no free parameters left in the model.

$\Gamma_{out}$  and  $\Gamma_{in}$  as functions of  $\Delta T$  are shown in Fig. 13(a) and Fig. 13(b), respectively. The X-ray reflectivity technique, which has been used in Ref. [1], provides access to the laterally averaged electron-density profile  $\rho(z)$ ; consequently the adsorption is measured in units of the areal electric charge density  $e\text{\AA}^{-2}$ . In order to present the theoretical adsorption data in these units, we use for the electron-density of the bulk liquid MCH the value  $\rho_e = 0.26e\text{\AA}^{-3}$  and neglect the density of the vapor. For temperature differences in the range  $5\text{K} \lesssim \Delta T \lesssim 8\text{K}$  we identify the filling regime, i.e., within this range the theoretical data  $\Gamma_{in}(\Delta T)$  resemble a power-law growth  $\Gamma_{in} \propto \Delta T^{-\beta_p}$  with an *effective* exponent  $\beta_p \approx 2.4$ . This

effective exponent  $\beta_p$  turns out to increase with the pit size and for  $R/\sigma = 245$  and  $D/\sigma = 500$  we find  $\beta_p \approx 3.4$ . There is no obvious connection between the effective exponent  $\beta_p$  and the exponent  $\gamma(R, D)$ , which is introduced in Subsec. III A for the midpoint interfacial height. In Ref. [1] the value of effective exponent  $\beta_p \approx 3.4$  has been roughly estimated by using  $\gamma = 2$  (which is valid for infinitely deep parabolic wedges or pits) and the expression  $V(l_p^{(0)}) = \frac{\pi}{2}(Rl_p^{(0)})^2/D + \frac{\pi}{3}(R^2l_p^{(0)}/D)^{3/2}$  for the volume enclosed between the surface of parabolic pit and a spherical meniscus [1, 5] which approximates the shape of the interfacial profile. With this, for the experimentally relevant values of  $l_p^{(0)}$  the dependence of  $V$  on  $\Delta\mu$  can be approximated as  $V(l_p^{(0)}) \sim \Delta\mu^{-2} \sim \Delta\mu^{-3.4}$  [1].

At  $\Delta T \approx 8\text{K}$  one can identify a small change in slope of the  $\Gamma_{in}(\Delta T)$  curve. This crossover corresponds to the disappearance of the interfacial meniscus, such that for larger values of  $\Delta T$  the interface follows the substrate shape. The authors of Ref. [1] assigned the value  $\beta_p \approx 0.76$  to their data. We explain this disagreement with the value  $\beta_p \approx 2.4$  reported here (see Fig. 13(b)) by a mislocation of the filling regime for the experimental data of  $\Gamma_{in}(\Delta T)$  induced by the large error bars for the data points at large  $\Delta T$ . There also seems to be a difference between the behavior of the theoretical and experimental results for  $\Gamma_{out}$  at large  $\Delta T$  (see Fig. 13(a)). However, for such large undersaturations the wetting film is only ca.  $10\text{\AA}$  thick causing rather large experimental error bars (actually larger [24] than those presented in Fig. 13(a) which are taken from Ref. [1]) for extracting values for the adsorption  $\Gamma_{out}$  from the scattering data. On the other hand, for such thin wetting films the reliability of our theoretical description is expected to deteriorate, too. Due to packing effects the use of an effective interface Hamiltonian should be replaced by a full-fledged density functional approach.

In Fig. 14 the laterally averaged interfacial profile  $\bar{l}_p(\Delta T)$  is shown. In order to obtain the experimental curve  $\bar{l}_p$ , first we have interpolated the experimental data for  $\Gamma_{in}$  and  $\Gamma_{out}$ , second we have formed  $\Gamma = \Gamma_{in} + \Gamma_{out}$ , and by using Eq. (27) we have determined  $\bar{l}_p(\Delta T)$ . This experimental curve is compared with the corresponding theoretical one. The theoretical curve for  $\bar{l}_p$  reveals the filling and postfilling scaling regimes, as well as the extended crossover to the planar scaling regime. Due to the relatively small depth  $D/\sigma \approx 36$  of the pits the crossover region between the first two regimes is rather extended. In the postfilling scaling regime, i.e., for  $0.7\text{K} \lesssim \Delta T \lesssim 4\text{K}$ , we obtain very good agreement between the experimental and theoretical data, while there are substantial deviations in the filling regime. With respect to the latter one we suggest that for deeper pits the experimental identification of the filling regime would be easier and the error bars smaller. First under this conditions the filling regime occurs over a wider range of undersaturations; second, the midpoint interfacial height attains larger values; third, the crossover to the postfill-

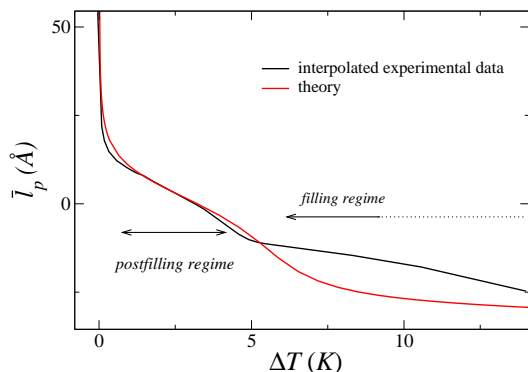


FIG. 14: Laterally averaged interfacial profile  $\bar{l}_p(\Delta T)$  for parabolic pits, obtained according to Eq. 27. The black line interpolates the experimental data from Ref. [1] (without error bars), and the red line denotes corresponding theoretical results.  $\Delta T$  is proportional to  $\Delta\mu$  (see the main text after Eq. (33)).

ing regime becomes more pronounced.

## V. SUMMARY AND OUTLOOK

Within an effective interface Hamiltonian approach based on density functional theory (Sect. II) we have studied complete wetting of four classes of solid substrates topographically patterned on the nanoscale: quadratic (and hexagonal) lattices of cylindrical or parabolic pits and periodic arrays of rectangular or parabolic grooves (Fig. 1). The long-ranged fluid-fluid interaction (giving rise to the bulk phase diagram shown in Fig. 2) and the fluid-substrate potential are modelled by isotropic pair potentials decaying with distance  $\sim 1/r^6$ . By analyzing the full range of undersaturations  $\Delta\mu$  relative to liquid-vapor coexistence in the bulk we have identified four different regimes for the increase of the wetting film thickness (Subsecs. III A and III B), and the existence of so-called covariances relating this increase for pits and grooves (Eq. (2)).

The filling of a cavity (Fig. 3) by the liquid occurs independently of the presence of other ones. This suggests that, e.g., in the filling regime the power law increase of the excess coverage in parabolic cavities is not only accessible to X-ray scattering (which requires periodic arrays) but also to AFM techniques applied to single cavities (see, e.g., Ref. [25]). For  $D/R \gtrsim 0.5$  (see Fig. 1) there exists a range of undersaturations, which we call

the postfilling scaling regime, in which the local interfacial characteristics, obtained for all four patterns, can be expressed in terms of a *single* scaling function (Eqs. (1), (2), (25), and (26) and Figs. 4, 5, and 7). However, the characterization of the laterally averaged interfacial profile requires *two* different scaling functions, one for pits and one for grooves (Figs. 8 and 9). All these scaling functions are independent of the cavity depth (Fig. 6).

For small undersaturations, the increase of the wetting film thickness is determined by the entire array of cavities. In the case of vertical cavity walls, i.e., for rectangular grooves and cylindrical pits, the interfacial thickness increases as on a planar substrate, but with an effective, geometry-dependent, Hamaker constant (Eq. 3 and Figs. 10-12). For very small undersaturations the patterns on the substrate become irrelevant, and the wetting film thickness increases as if the substrate would be flat. The crossover to this latter so-called planar scaling regime occurs only for long-ranged dispersion forces. For short-ranged interactions, instead, the increase of the wetting film thickness would remain determined by the areal fraction of the solid at the substrate surface  $z = 0$  for *all* film thicknesses [26].

We have been able to report quantitative agreement between our theory and the X-ray scattering data of Ref. [1] (Figs. 13 and 14). For the range of undersaturations corresponding to the postfilling scaling regime, the agreement is satisfactory (Fig. 14). We have been able to clarify the interpretation of the adsorption parabolic pits in terms of an effective filling exponent  $\beta_p$  (Fig. 13(b)). We suggest, that for deeper pits the experimental identification of the filling regime would be easier. In order to test our scaling predictions (Eqs. (1) and (2)) experiments for the following surface structures are still missing: (i) patterns with cavities of different sizes have to be considered; (ii) resolving the full morphology of the wetting films, or at least determining the midpoint interfacial heights, are highly desirable.

A natural extension of the work presented here would be to study the temperature dependence of the filling regime and of the scaling function for the postfilling scaling regime. Another perspective is to consider substrates patterned by, e.g., cylindrical nanoposts.

## Acknowledgments

M.T. gratefully acknowledges helpful discussions with M. N. Popescu.

- 
- [1] O. Gang, K. J. Alvine, M. Fukuto, P. S. Pershan, C. T. Black, and B. M. Ocko, Phys. Rev. Lett. **95**, 217801 (2005).  
 [2] L. Bruschi, A. Carlin, and G. Mistura, Phys. Rev. Lett.

**89**, 166101 (2002).

- [3] L. Bruschi, G. Fois, G. Mistura, M. Tormen, V. Garbin, E. di Fabrizio, A. Gerardino, and M. Natali, J. Chem. Phys. **125**, 144709 (2006).

- [4] K. Rejmer, S. Dietrich, and M. Napiórkowski, Phys. Rev. E **60** 4027 (1999).
- [5] C. Rascón and A. O. Parry, Nature **407**, 986 (2000);
- [6] C. Rascón and A. O. Parry, J. Chem. Phys. **112**, 5157 (2000).
- [7] C. Rascón and A. O. Parry, Phys. Rev. Lett. **94**, 096103 (2005).
- [8] M. Tasinkevych and S. Dietrich, Phys. Rev. Lett. **97**, 106102 (2006).
- [9] S. Dietrich, in *Phase Transitions and Critical Phenomena*, edited by C. Domb and J. L. Lebowitz (Academic, London, 1988), Vol. 12, p. 1.
- [10] S. Dietrich and M. Napiórkowski, Phys. Rev. A **43** 1861 (1991).
- [11] G. A. Darbellay and J. M. Yeomans, J. Phys. A: Math. Gen. **25**, 4275 (1992).
- [12] M. O. Robbins, D. Andelman, and J. F. Joanny, Phys. Rev. A **43**, 4344 (1991).
- [13] M. Napiórkowski, W. Koch, and S. Dietrich, Phys. Rev. A **45**, 5760 (1992).
- [14] W. Koch, S. Dietrich, and M. Napiórkowski, Phys. Rev. E **51**, 3300 (1995).
- [15] C. Bauer and S. Dietrich, Phys. Rev. E **60**, 6919 (1999); **61**, 1664 (2000); C. Bauer, S. Dietrich, and A. O. Parry, Europhys. Lett. **47**, 474 (1999).
- [16] R. Evans, Adv. Phys. **28**, 143 (1979).
- [17] J. D. Weeks, D. Chandler, and H. C. Andersen, J. Chem. Phys. **54**, 5237 (1971).
- [18] S. Dietrich and M. Napiórkowski, Physica A **177**, 437 (1991); M. Napiórkowski and S. Dietrich, Z. Phys. B **89**, 263 (1992); Phys. Rev. E **47**, 1836 (1993).
- [19] N. F. Carnahan and K. E. Starling, J. Chem. Phys. **51**, 635 (1969).
- [20] K. R. Mecke and S. Dietrich, Phys. Rev. E **59**, 6766 (1999).
- [21] C. Bauer and S. Dietrich, Eur. Phys. J. B **10**, 767 (1999).
- [22] S. Goldman, J. Phys. Chem. **80**, 1697 (1976).
- [23] J. J. Jasper, J. Phys. Chem. Ref. Data, **1**, 841 (1972).
- [24] O. Gang, P. S. Pershan, and B. M. Ocko, private communication; see also O. Gang, K. J. Alvine, M. Fukuto, P. S. Pershan, C. T. Black, and B. M. Ocko, Phys. Rev. Lett. **97**, 039902 (2006).
- [25] K. Fukuzawa, J. Kawamura, T. Deguchi, H. Zhang, and Y. Mitsuya, J. Chem. Phys. **121**, 4358 (2004).
- [26] L. Harnau, F. Penna, and S. Dietrich, Phys. Rev. E **70**, 021505 (2004).